

Neural-network-based depth-resolved multiscale structural optimization using density functional theory and electron diffraction data

Robert S. Pennington,^{1,*} Catalina Coll,^{2,3} Sònia Estradé,^{2,3} Francesca Peiró,^{2,3} and Christoph T. Koch¹

¹*AG Structure Research and Electron Microscopy, Institut für Physik, Humboldt-Universität zu Berlin, 12489 Berlin, Germany*

²*Laboratory of Electron Nanoscopies (LENS-MIND), Departament d'Enginyeries: Electrònica, Universitat de Barcelona, Barcelona, Spain*

³*Institute of Nanoscience and Nanotechnology (IN2UB), Universitat de Barcelona, Spain*



(Received 2 December 2016; published 24 January 2018)

Iterative neural-network-based three-dimensional structural optimization of atomic positions over tens of nanometers is performed using transmission electron microscope (TEM) diffraction data simulated from density functional theory (DFT) all-electron densities, thus retrieving parameter variations along the beam direction. We first use experimental data to show that the GPAW DFT code's all-electron densities are considerably more accurate for electron diffraction calculations compared to conventional isolated-atom scattering factors, and they also compare well to Wien2K DFT simulations. This DFT-TEM combination is then integrated into an iterative neural-network-optimization-based algorithm (PRIMES, parameter retrieval and inversion from multiple electron scattering) to retrieve nanometer-scale ferroelectric polarization domains and strain in theoretical bulklike specimens from TEM data. DFT and isolated-atom methods produce substantially different diffraction patterns and retrieved polarization domain parameters, and DFT is sufficient to retrieve strain properties from a silicon specimen simulated using experimentally derived structure factors. Thus, we show that the improved accuracy, fast computation, and intuitive integration make the GPAW DFT code well suited for three-dimensional materials characterization and demonstrate this using an iterative neural-network algorithm that is verifiable on the mesoscale and, with DFT integration, self-consistent on the nanoscale.

DOI: [10.1103/PhysRevB.97.024112](https://doi.org/10.1103/PhysRevB.97.024112)

I. INTRODUCTION

Experimental transmission electron microscopy (TEM) and computational density functional theory (DFT) are both well-established tools for nanoscale materials physics—TEM characterizes materials with Angstrom-scale spatial resolution [1,2], and DFT simulates electronic structure, including for atomic-position relaxation into minimum-energy configurations [3]. Conceptually, DFT and TEM are easily linked—DFT-generated charge densities (all-electron charge densities plus nuclei) can provide specimen models for TEM simulations of images or diffraction patterns. This DFT-TEM combination can benefit both techniques. For TEM, DFT electronic structure could replace isolated-atom-scattering-factor (IASF) models, which are common but completely exclude chemical bonding [4,5]. For DFT, experimental TEM data can map large non-minimum-energy structures, including strain or ferroelectric domains, that might be problematic for DFT alone [6,7]. Previous DFT-TEM combinations have been rare and, when attempted, have generally assumed a depth-invariant bulklike TEM specimen, or very thin crystals for high-resolution imaging [8–13]. For example, DFT-TEM high-resolution image simulations of picometer-scale atomic shifts in BaTiO₃ showed general consistency between experimental and DFT results, but their simulations assumed depth invariance and they cautioned about interpreting thin-crystal results as bulklike [9]. To be widely used, a DFT-TEM combination must be not only

more accurate than IASF models, but also easy to integrate into TEM simulations, fast enough for applications using iterative algorithms, and able to deal with non-depth-invariant specimens (e.g., depth-dependent polarization domains). In this paper, we first show that the GPAW (grid-based projector-augmented wave) DFT code [14,15] is a good candidate for TEM simulations; for TEM-relevant quantities, GPAW's all-electron densities are accurate and accessible, and we directly compare GPAW to both the Wien2K DFT code and experimental quantities. We then show that GPAW DFT is fast enough to be integrated into PRIMES (parameter retrieval and inversion from multiple electron scattering), our iterative three-dimensional parameter-retrieval artificial-neural-network algorithm [16–18], retrieving depth-direction polarization variations on a BaTiO₃ simulated specimen and strain from a Si simulated specimen. This algorithm provides a way to extend and benchmark DFT codes against a wide range of large physical structures. In summary, we present both a DFT-TEM-based three-dimensional characterization method that is self-consistent on the nanoscale and verifiable on the mesoscale and benefits both DFT and TEM research, and we also present a straightforward way to use accurate DFT electronic structure for TEM simulations.

TEM image and diffraction-pattern simulations are a natural application for DFT-generated ground-state charge densities, especially using the GPAW DFT code. There are good reasons to pursue DFT for TEM applications: Electron-holographic mean inner potentials (MIPs) from ground-state simulations have been consistent both between different DFT codes and experimental data [19–21]. The two main TEM simulation

*Corresponding author: robert.pennington@physik.hu-berlin.de

algorithms are multislice and Bloch-wave, which represent the specimen as, respectively, real-space electrostatic potentials or reciprocal-space structure factors [22–27]. The open-source GPAW DFT code is ideal for TEM image and diffraction pattern simulations, because GPAW easily provides the all-electron density on a real-space grid via the `get_all_electron_density()` function, and the atomic nuclei positions are DFT inputs via the atomic simulation environment (ASE) [14,15,28]. The GPAW DFT code has been previously used to generate MIPs, including showing the MIP’s theoretical surface-state dependence [29] computationally using both thin-film and nanowire simulations [21]. We use the Bloch-wave approach and generate diffraction patterns, but processing GPAW charge densities for multislice would require only minor differences. For our Bloch-wave approach, we assume a locally-regular crystal, which enables both periodic boundary conditions on the DFT simulation and fast-Fourier-transform conversion from real-space electron density into reciprocal space. Converting between electron density plus nuclei positions and TEM structure factors is described in textbooks, using the Mott-Bethe equation [30]. Within the Bloch-wave formalism, multiple scattering means that a matrix exponential is required to convert the structure factors into an electron scattering matrix. The stacked-Bloch-wave implementation represents the specimen as a sequence of scattering matrices, enabling easy, small-unit-cell simulation for specimens that change along the beam direction [31,32]. Because these stacked scattering matrices do not multiplicatively commute with each other, the stack order can be retrieved from TEM measurement data (e.g., convergent-beam electron diffraction [CBED] patterns)—meaning specimen properties that vary along the beam direction, including strain and ferroelectric polarization, have been retrieved from simulated CBED data with depth resolution down to 2.5 nm at 300 kV using the PRIMES algorithm [16–18]. However, this algorithm relies on the simulation’s specimen charge density model being close to the actual specimen; DFT provides a self-consistent and realistic charge density model suitable for three-dimensional specimens, unlike conventional techniques.

Conventional TEM simulation methods typically rely on non-DFT charge density models that are unphysical or impractical, especially for unknown samples or advanced, three-dimensional applications. The most common method uses isolated-atom scattering factors (IASFs), which represent the specimen as a set of noninteracting isotropic atoms. IASFs are unphysical because they completely neglect chemical bonding between atoms; this leads to inaccuracies like the IASF silicon (222) structure factor being zero due to symmetry, disagreeing with both experimental measurements and DFT simulations [33,34]. In some cases, structure factors have been directly fitted to experimental CBED and CBED-like data from benchmark materials, leading to two-dimensional charge density or potential maps from experimental TEM data [8,34–37]. However, a specimen with three-dimensional features is problematic for direct fitting, both because each individual layer would require structure-factor fitting, requiring many independent variables that are not self-consistent, and also because individual structure factors will be depth-sensitive, so direct fitting may not be equally accurate over the entire specimen [38]. Therefore, in the rest of this paper, we

show that GPAW DFT is a logical fit for three-dimensional TEM specimens because it is easy to use, accurate compared to IASF, and fast enough to use in an iterative routine like PRIMES. For DFT-focused research, our parameter-retrieval algorithm is also one way for DFT platforms to self-consistently explore nanoscale behavior unfolding on the mesoscale, with possible experimental verification or benchmarking against other codes.

II. RESULTS

In the following sections, we simulate silicon structure factors and electron diffraction data, and demonstrate silicon and tetragonal BaTiO₃ three-dimensional parameter retrieval. We use GPAW version 0.10 and ASE version 3.8.1. Simulations are performed both including and excluding isotropic Debye-Waller factors and absorption; when absorption is excluded, the total electron dose on the specimen and detector planes is equal. For silicon, unless otherwise specified, we used a bulk unit cell with the experimental lattice parameter $a = 5.431 \text{ \AA}$ [39] and 100 kV accelerating voltage, for DFT simulations $k = 4^3$ k points and $g = 24^3$ grid points, and, for IASF simulations, the Lobato *et al.* IASF parametrization [5], which compared well with other IASF parametrizations [40]. For tetragonal BaTiO₃, $\{a, c\} = \{3.9925, 4.0365\} \text{ \AA}$ [41], DFT $k = 4^3$ and $g = 24^3$, with 289 beams (the zero- and first-order Laue zones for the [111] zone axis with excitation error $s \leq 1.00 \text{ nm}^{-1}$ at 100 kV). Our multi-CPU, multi-GPU code calculates scattering matrices using GPU-accelerated matrix exponentials [32] and allocates pattern subsections to different computational threads using OpenMPI [42]. The PRIMES algorithm, described elsewhere, uses optimization techniques from artificial neural network theory to perform multiple-scattering inversion for crystalline specimens [16], samples a region of reciprocal space without tilting the specimen [17], and can efficiently retrieve ferroelectric polarization and strain [18]. Consistent with a large-angle rocking-beam electron diffraction (LARBED) pattern, we sample a ($2^\circ \times 2^\circ$) reciprocal-space span (0.1° dot-pitch), centered on the [111] zone axis for a total of 441 reciprocal-space points [43]. Other simulation conditions are used as noted.

A. Structure-factor generation methods, compared

In this section, IASF and DFT structure-factor generation methods are compared against each other and against experimental structure factors. We directly compare both structure factors and electron-diffraction pattern intensities, both with and without absorption, and, in the following section, including two different DFT codes. Simulations without absorption provide quantitative thickness-independent assessment of the effect of DFT alone, while simulations with absorption provide a test of the standard Bird-King absorption model combined with DFT elastic scattering. We use patterns generated from experimentally fitted structure factors instead of experimental diffraction patterns because comparing structure factor models requires knowing the correct “ground truth” values. We show that DFT elastic structure factor models improve the accuracy of both structure factors and electron diffraction patterns, and that DFT models correspond to experimental data far better than IASF elastic structure factors.

TABLE I. Silicon structure factors $|V_g|$ for elastic electron scattering, in volts: experiment compared with IASF and DFT. Experimental values and parameters are from the literature [34], with the Debye-Waller factor zeroed. IASF values use the Lobato *et al.* isotropic parametrization [5]. DFT values use the GPAW-provided LDA (local density approximation) [3], PBE (Perdew-Burke-Ernzerhof) [44], revPBE [45], and RPBE [46] exchange-correlation functionals.

g	Exp.	IASF	LDA	PBE	revPBE	RPBE
$\langle 111 \rangle$	5.215	5.510	5.204	5.201	5.201	5.201
$\langle 220 \rangle$	4.486	4.457	4.495	4.500	4.504	4.505
$\langle 311 \rangle$	2.583	2.531	2.585	2.586	2.587	2.587
$\langle 222 \rangle$	0.112	0.0 ^a	0.095	0.097	0.097	0.097
$\langle 400 \rangle$	2.752	2.739	2.757	2.754	2.753	2.753
$\langle 331 \rangle$	1.673	1.713	1.697	1.695	1.694	1.694
$\langle 422 \rangle$	2.005	2.052	2.048	2.044	2.044	2.043

^aZero due to IASF symmetry.

First, we compare the structure-factor values directly. We demonstrate GPAW's accuracy for elastic structure factors by comparing against IASF and experimental structure factors from the literature [34], shown in Table I and Table II. Compared to IASF, DFT is a much more accurate match to the experimental structure factors found via direct fitting. In fact, DFT's increasing mismatch at higher g could be an artifact of the experimental data analysis, because Ogata *et al.* fit both structure factors and the Debye-Waller factor [34]; Debye-Waller-factor misdetermination would be g dependent, like this is. Thus, DFT could improve experimental Debye-Waller fitting, as well, by providing a self-consistent model for low-order structure factors. While the differences shown in Table I and Table II appear small, Fig. 1 shows a Si CBED pattern with IASF or DFT structure factors, where the choice of structure factor substantially affects the pattern intensity, including outside the central [000] disk. Using inaccurate structure factors can easily lead to data misinterpretation. For accurate, quantifiable simulations, DFT is a clear first resort over IASF, both conceptually and practically, and improving structure factors can yield substantial measurable effects.

Now, we compare CBED patterns generated using IASF, DFT, and experimental structure factors, both with and without inelastic structure factors to model beam attenuation. Inelastic structure factors correspond to different physical properties

TABLE II. Differences between the experimental and simulated $|V_g|$ values shown in Table I. DFT $|V_g|$ values are much closer to experimental measurements than IASF $|V_g|$ values are. $\langle 222 \rangle$ is nonzero both experimentally and with DFT, but zero in IASF calculations due to symmetry.

g	IASF	LDA	PBE	revPBE	RPBE
$\langle 111 \rangle$	5.65%	0.21%	0.28%	0.26%	0.28%
$\langle 220 \rangle$	0.65%	0.20%	0.32%	0.39%	0.41%
$\langle 311 \rangle$	2.04%	0.05%	0.09%	0.13%	0.14%
$\langle 222 \rangle$	(IASF zero, exp. & DFT nonzero)				
$\langle 400 \rangle$	0.48%	0.18%	0.06%	0.04%	0.03%
$\langle 331 \rangle$	2.35%	1.43%	1.29%	1.25%	1.24%
$\langle 422 \rangle$	2.33%	2.13%	1.95%	1.90%	1.89%

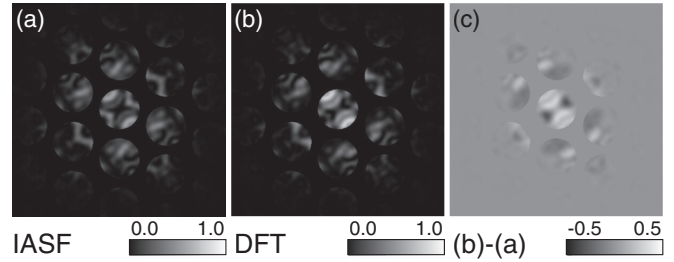


FIG. 1. Diffraction intensities for a simulated Si 100 nm [110] CBED pattern without absorption at 100 kV, showing that differences in elastic structure factor models can lead to substantial intensity changes. (a) Intensities calculated using IASF models. (b) Intensities calculated using DFT models. (c) Difference between (a) and (b); maximum single-pixel intensity difference 29.8%.

than elastic ones, as discussed in Sec. III. The Bird-King parameterized model for inelastic structure factors [47] yields close but approximate values [34]. We also compensated for total beam attenuation (which arises from the imaginary part of the structure-factor matrix diagonal) when including absorption by renormalizing all the patterns to the same overall attenuation; this would also be done for experimental data when calibrating the overall pattern intensity. Theoretically, this compensation is also necessary when using DFT because the DFT simulations have zero net charge (and, without a region of free space included, an undefined mean inner potential) [48] so the real part of the structure-factor matrix diagonal is zero, so the Bird-King absorption model doesn't correctly calculate total beam attenuation; we used our previous values for the Si mean inner potential to calculate the total beam attenuation [21,48]. We generated patterns using different structure factor models for visual comparison, including with and without absorption, and with and without

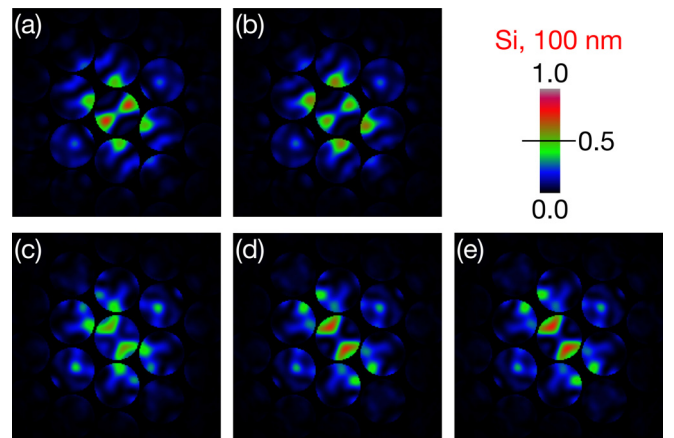


FIG. 2. CBED patterns [(1°×1°) span, disk radius 3.7 mrad] generated with different elastic structure factor models for 100 nm Si at 200 kV accelerating voltage ($n = 261$ beams). These patterns are generated with elastic structure factors only; inelastic scattering is shown in Fig. 3. (a) IASF model without Debye-Waller factors; (b) DFT model without Debye-Waller factors; (c) IASF with Debye-Waller factor ($M = 0.463$); (d) DFT with Debye-Waller factor ($M = 0.463$); (e) as (d), but with experimentally derived structure factors [34] for low-order scattering.

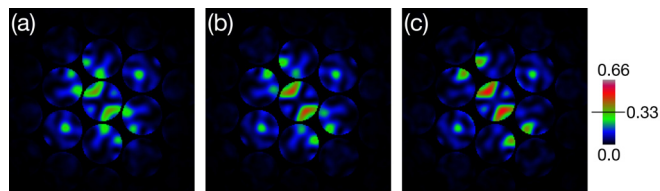


FIG. 3. As Figs. 2(c)–2(e), but with inelastic scattering. The Bird-King inelastic scattering factors are used [47], so the Debye-Waller factors must be nonzero. Beam attenuation is calculated from the scenario in (b), with the Bird-King inelastic scattering parameter applied to a DFT-calculated mean inner potential [21]. (a),(b) As Figs. 2(c) and 2(d), but with Bird-King inelastic scattering. (c) As (b), but with experimental structure factors for low-order inelastic and elastic scattering [34].

an experimentally derived Debye-Waller factor. Figure 2 and Fig. 3 show simulated CBED patterns using IASF, DFT, and experimental structure factors. When only elastic scattering is included, compared to experimentally-derived-structure-factor patterns, DFT yields much closer results than IASF; including the Debye-Waller factor both reinforces this and substantially changes the patterns. When inelastic scattering is included, DFT is still noticeably better than IASF models. However, these results mean that DFT-generated CBED patterns are likely to be closer matches to experimental CBED patterns, as long as a suitable Debye-Waller factor is used. We examine this further in later sections of this paper using both zone-axis thickness-determination comparisons and PRIMES retrieval performance.

Thickness determination performance can be used as another way of comparing different structure-factor models. CBED patterns change as a function of thickness, and the pattern differences visible in Figs. 1, 2, and 3 suggest that, for a given target pattern, using the wrong structure factor model might lead to the closest-match pattern being at the wrong thickness. Therefore, we examined two questions: First, if the thickness is known, what is the measurable intensity effect of using different structure-factor models (Fig. 4); second, if the

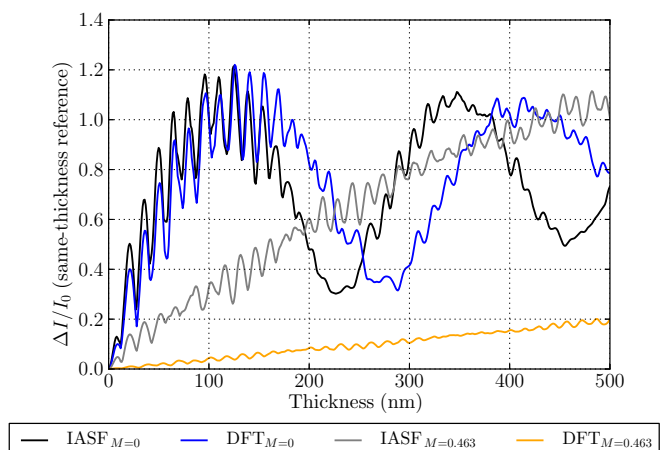


FIG. 4. Intensity mismatch across CBED patterns, compared to the experimental-structure-factor silicon 200 kV CBED pattern calculated using the same thickness without absorption.

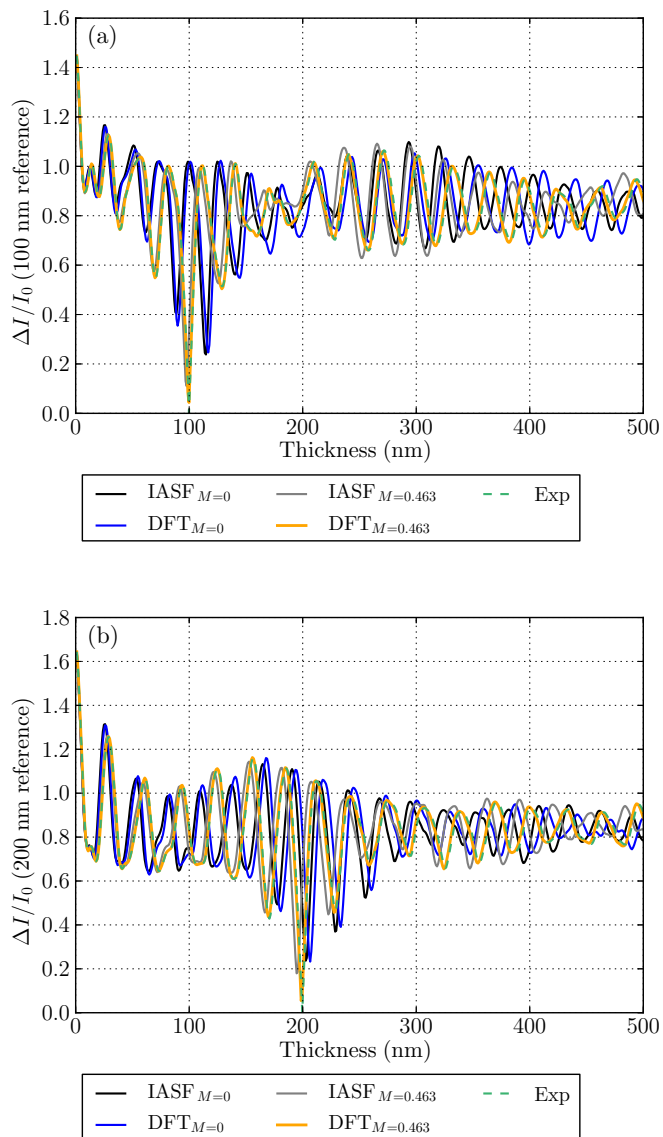


FIG. 5. Intensity mismatch against experimental-structure-factor silicon 200 kV CBED patterns without absorption at (a) 100 nm and (b) 200 nm. Lower mismatch means a closer pattern match.

thickness is unknown, how inaccurately would the thickness be determined using the different models (Fig. 5)? Figure 4 compares patterns at the same thickness generated with different structure-factor models, yielding two main points—first, Debye-Waller factors influence the diffraction patterns enough to be necessary for comparisons with experiment, and second, DFT performs much better than IASF. Figure 5 compares patterns across different thicknesses with the pattern at one single thickness [either (a) 100 nm or (b) 200 nm], reinforcing those two points and adding a third: The “best-fit” IASF pattern is at the wrong thickness entirely, while the best-fit DFT pattern is close. Extending this further, Fig. 6 compares best-fit thicknesses as a function of true thickness for different techniques (the minima from each curve in Fig. 5 would yield the individual data points at 100 and 200 nm), showing that including both the correct Debye-Waller factor and a DFT simulation would yield a very close thickness

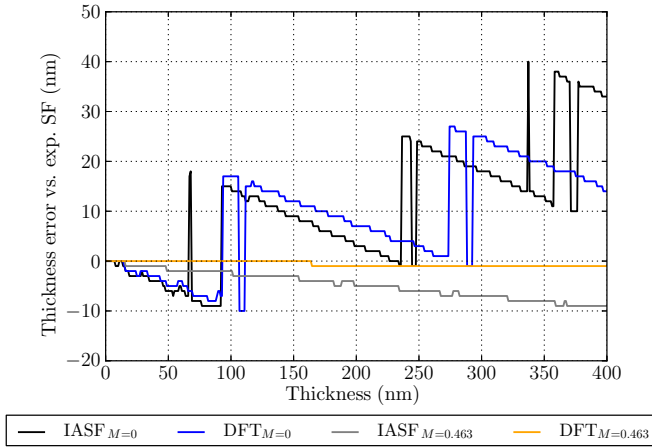


FIG. 6. Thickness misdetermination against experimental-structure-factor silicon 200 kV CBED patterns without absorption, under the same conditions as Figs. 4 and 5. The result is the error in the best-fit pattern's thickness. (I.e., 0 represents a correct thickness match.) This is a graph of the minima locations from Fig. 5 but for more than just those two thicknesses. Including the correct Debye-Waller factor greatly improves the fit; however, DFT provides a noticeable improvement compared to IASF models, and the DFT matches are almost all correct within 1 nm for thicknesses up to 400 nm.

determination. Thus, IASF methods may misdetermine the specimen thickness, while DFT will be much closer. We discuss inelastic structure factor effects in the next section, when we compare different DFT codes.

B. Using different DFT codes for structure-factor generation

Because different DFT implementations are available, we compared two different DFT codes—GPAW and Wien2K [49]—by generating CBED patterns from different materials. Both Wien2K and GPAW have been used for mean inner potential calculations on comparable materials [20,21]. Wien2K has been used previously for comparisons with TEM experimental data [20]; however, unlike GPAW, Wien2K is not freely available and would be more difficult than GPAW to integrate into TEM analysis, including PRIMES or other routines that natively use the Python programming language, especially those that depend on the ASE library. The Wien2K simulations used the linearized augmented plane wave (LAPW) method with the local density approximation (LDA) and later improved using the modified Becke-Johnson potential (mBJ) for silicon and diamond. For the systems with strongly correlated electronic states, strontium titanate ($a = 3.905 \text{ \AA}$) and barium titanate, LDA+ U has been used, which is based on a corrective functional inspired by the Hubbard model; U corresponds to an effective energy which is added to the more correlated electronic states (d and f orbitals). The cutoff energy was set at 12 Ry to handle the maximum number of electronic states as valence/semicore. For both Wien2K potentials, self-consistent field (SCF) cycles of the crystal were performed until the total energy was converged to 10^{-5} eV with 1000 k points.

The results from comparing GPAW and Wien2K using electron diffraction simulations show that the two DFT

TABLE III. Elastic structure factors simulated using GPAW and Wien2K, in volts, as in Table I. The first row corresponds to the LDA column in Table I.

g	(111)	(220)	(311)	(222)	(400)	(331)	(422)
Si [†]	5.204	4.495	2.585	0.095	2.757	1.697	2.048
Si*	5.154	4.515	2.602	0.128	2.756	1.687	2.040
C [†]	6.552	5.149	2.831	0.095	2.840	1.693	1.949
C*	6.510	5.211	2.871	0.137	2.853	1.686	1.942
g	(110)	(211)	(220)	(321)	(330)	(422)	
BaTiO ₃ [‡]	7.845	4.362	6.276	2.589	2.190	2.952	
BaTiO ₃ **	7.818	4.365	6.280	2.589	2.190	2.955	
BaTiO ₃ [†]	7.749	4.354	6.275	2.590	2.190	2.952	
SrTiO ₃ [‡]	6.500	3.505	5.668	2.063	1.736	2.614	
SrTiO ₃ **	6.469	3.508	5.671	2.061	1.735	2.615	
SrTiO ₃ [†]	6.407	3.498	5.667	2.064	1.737	2.614	

[†]GPAW, LDA.

*Wien2K, LDA.

[‡]GPAW, LDA+ U (0.52 Ry).

**Wien2K, LDA+ U (0.52 Ry).

codes largely agree. Table III shows that both DFT methods agree on their structure factors for multiple materials. Table III also demonstrates that using a DFT+ U method (LDA+ U exchange-correlation functional) influences primarily the lowest-order structure factors, compared to a LDA functional. Thus, TEM can also be used to compare different DFT+ U parameters. When these structure factors are applied to CBED pattern generation, Fig. 7 shows that the resulting patterns closely agree. This agreement holds even when absorption is included, and compared to IASF models, the differences between different DFT methods are minimal.

Figure 8 compares different codes' intensities when including absorption. First, the differences between codes are much smaller (red line) than the differences between the DFT results and the experimentally derived structure factor results (blue lines). GPAW and Wien2K are approximately the same accuracy, but the details are somewhat different, as shown by the red line being larger than the naive difference between the two blue lines, arising because different parts of the patterns match, as shown in Fig. 7. Thus, we show that different DFT codes generate similar CBED patterns, consistent with previous results showing that different DFT codes generate similar mean inner potentials [21]. This demonstrates that different DFT implementations can benchmark and compare accuracy using TEM simulation methods, including CBED pattern intensities, and that different DFT codes can yield very similar and consistent results.

C. Iterative methods: Ferroelectric polarization retrieval using PRIMES and GPAW DFT

Now, we use iterative GPAW DFT calculations with TEM data to perform iterative structural optimization for non-minimum-energy structures. As mentioned above, the parameter-retrieval method used, PRIMES, is described in detail elsewhere [16–18]. The layered polarization structure, seen in Figs. 9(a) and 9(b), is a non-minimum-energy structure, because DFT-calculated polarized and unpolarized BTO unit cells have different energies. Examples of the diffraction data

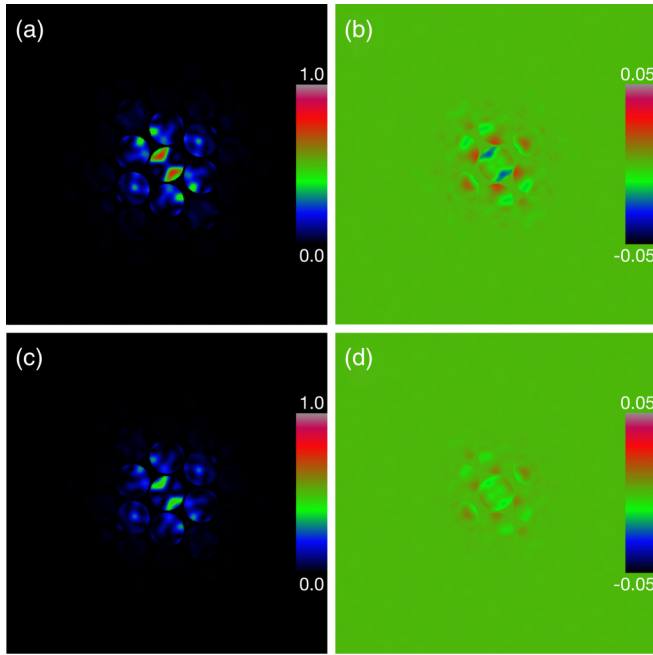


FIG. 7. Comparison between GPAW and Wien2K using intensity-normalized CBED patterns at 200 kV with Debye-Waller factors and with and without absorption. (a) Wien2K pattern without absorption, under the same conditions as the GPAW pattern in Fig. 2(d) and (b) difference between (a) and Fig. 2(d). (c) Wien2K pattern with absorption, under the same conditions as the GPAW pattern in Fig. 3(b) and (d) difference between (c) and Fig. 3(b).

used are shown in Figs. 9(c) and 9(d), corresponding to a large-angle rocking-beam electron diffraction (LARBED) dataset [43]; the left-right difference shows how the polarization atomic displacements can affect pattern intensities. Figure 9(e) shows how DFT and IASF can yield measurably different diffraction intensities. Figure 10 shows the retrieved polarizations for each 10 nm layer as a function of simulation iteration, showing that a DFT-based approach can be used iteratively to

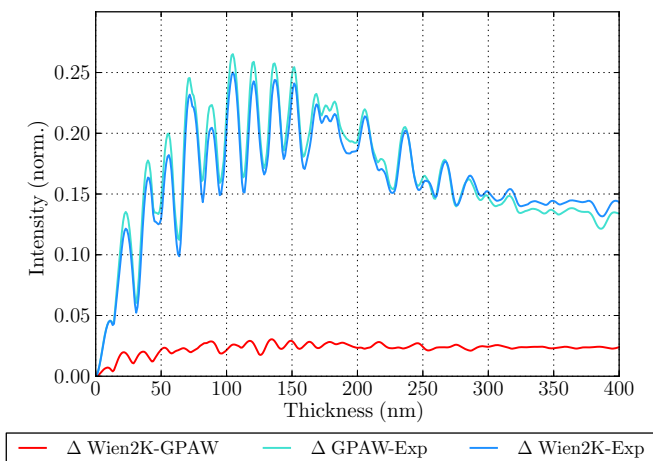


FIG. 8. Thickness comparison of CBED pattern intensities (including absorption) between Wien2K and GPAW (red line) and compared against experimental-structure-factor pattern intensities (both blue lines).

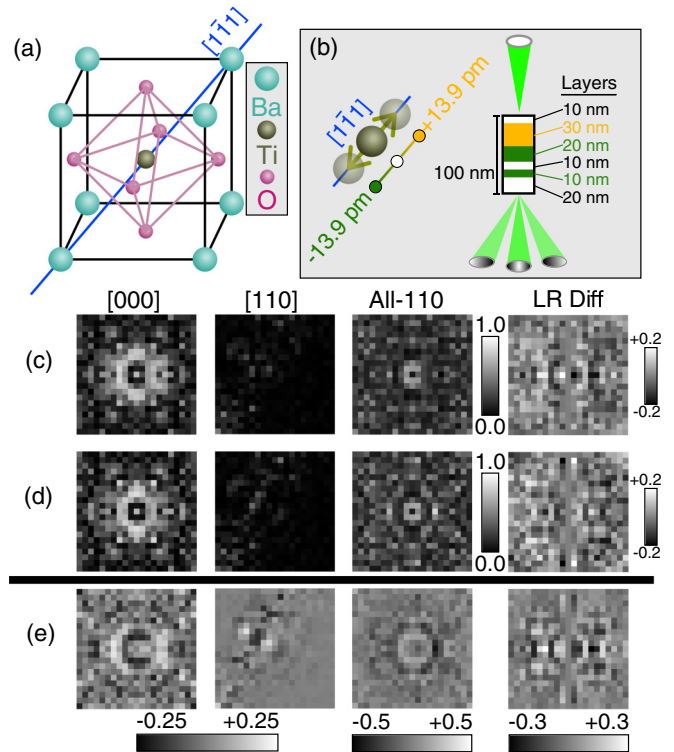


FIG. 9. BaTiO₃ (a) unit cell and (b) specific polarization domain specimen used for PRIMES in this work, with multiple different polarized domains and schematic diagram of the CBED technique. (c) Simulated intensity results for the specimen in (b) generated using isolated-atom scattering factor (IASF) models and parameters as given in the text—left-to-right, the direct beam, one 110 reflection, the six summed 110 reflections (“All-110”), and the difference between the left and right sides of the “All-110” image shows polarization effects. (d) As (c) but using DFT models instead of IASF. (e) Difference between (c) and (d)—demonstrating that DFT models produce substantially different intensity patterns than IASF models.

determine this non-minimum-energy structure. Interestingly, Fig. 11 shows that using the IASF model retrieves the wrong polarizations for a DFT-generated specimen, reinforcing the above conclusion that accurate structure factors matter, especially for iterative methods. Figure 12 shows that, for a DFT-generated specimen, the DFT approach converges well on the true answer, and would be experimentally noise-limited, while the IASF model is inaccurate.

This iterative approach is also computationally tractable—on our 16-core computer, the DFT approach required about 17 hours for the 2000 DFT calculations plus approximately a half hour for the GPU-accelerated TEM simulations. In principle, non-minimum-energy structures stretching over tens or hundreds of nanometers can be characterized using a combination of TEM and DFT, and TEM simulations can use DFT instead of IASF models.

D. Iterative methods: PRIMES structure-factor-model sensitivity

Now, we explore how the PRIMES algorithm handles a realistic structure-factor model, including experimentally

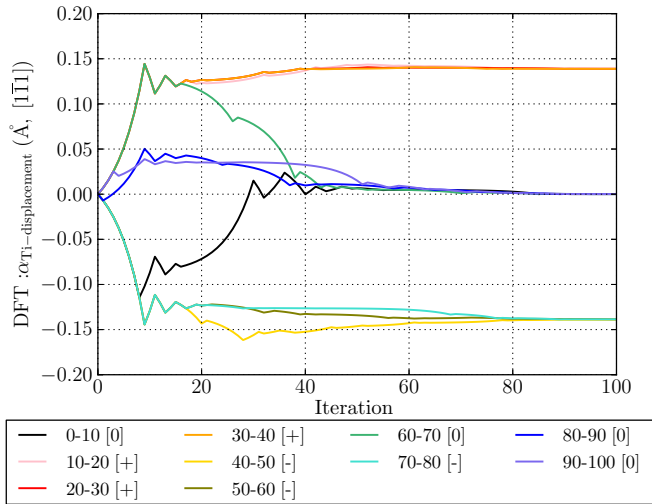


FIG. 10. PRIMES-retrieved polarization parameters for the DFT specimen model against the DFT-generated target. The legend indicates both the correct polarization value (+, −, or 0) and the layer’s depth in nm. PRIMES successfully retrieves the polarization in every layer. The mean parameter error from here is the dashed blue line in Fig. 12.

fitted structure factors and inelastic scattering. While inelastic scattering is not typically used for PRIMES benchmarks because inelastic scattering introduces thickness dependence to the error metric, we extend our analysis to include inelastic scattering as a full test of our *ab initio* approach. Correctly benchmarking PRIMES requires exact knowledge of the target specimen for quantification of the retrieved-parameter error. Using the strain components corresponding to crystal tilt, as we used previously to introduce PRIMES [16], enables

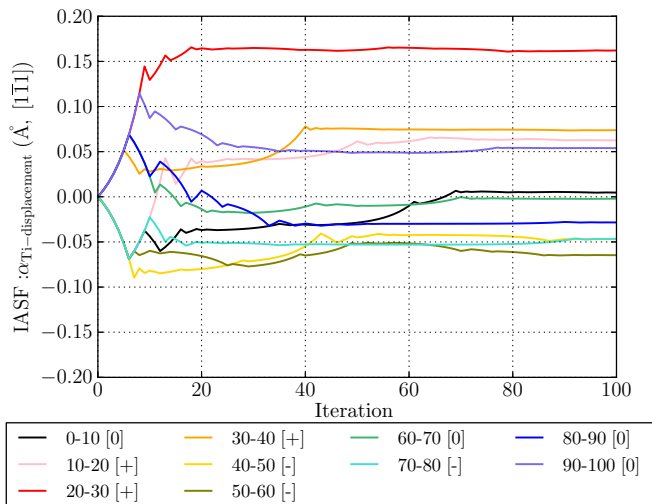


FIG. 11. PRIMES-retrieved polarization parameters for the IASF specimen model against the DFT-generated target. Unlike when the DFT specimen model is used, the retrieved parameters are incorrect (correct values are shown in Fig. 10). This shows that neglecting chemical bonding can result in retrieving incorrect specimen parameters. The mean parameter error from here is the dashed red line in Fig. 12.

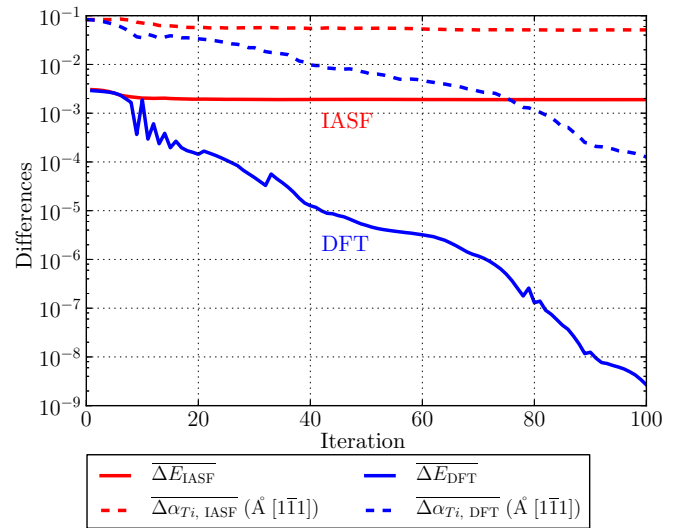


FIG. 12. PRIMES results against a DFT-generated target, using either a DFT specimen model (blue) or a IASF specimen model (red), showing that the IASF specimen model fails to accurately match the DFT-generated target. Solid lines show the mean measurement mismatch between the candidate and target diffraction data. Dashed lines show the mean error in atomic displacements between the retrieved specimen and the true specimen.

using unmodified experimental structure factors (no unit cell distortions or atomic displacements). This is also a large non-minimum-energy structure, like the ferroelectric polarization test case discussed earlier. By including inelastic scattering, a Debye-Waller factor, and DFT-generated elastic structure factors in our model, and comparing against data generated from experimental structure factors, this scenario provides guidance on PRIMES performance using realistically achievable structure-factor models.

Figure 13 shows the result of using PRIMES with a generated silicon specimen model derived from experimental structure factors. The silicon specimen has sequentially changing strain as a function of depth, divided into 11 distinct 10-nm-thick layers with 0.02° crystal tilt between each. PRIMES is able to retrieve the correct values with an average error of approximately 0.01° , thus successfully discriminating between layers. We note that, because these tests include absorption, beam attenuation makes the error metrics thickness dependent.

This test shows that PRIMES, using available models, can successfully retrieve specimen parameters from a realistic structure-factor target and that DFT retrieval is much closer to the experimental case than it was to the IASF case in the previous section.

III. ANALYSIS

These results demonstrate the substantial scope for future DFT-TEM combinations, especially to understand three-dimensional nano-to-mesoscale structures. For TEM simulations, open-source GPAW’s `get_all_electron_density()` function yields an electron density that is easy to integrate into existing TEM simulation routines, yields substantial accuracy improvements compared to IASF models, and is fast enough to integrate into iterative TEM simulation

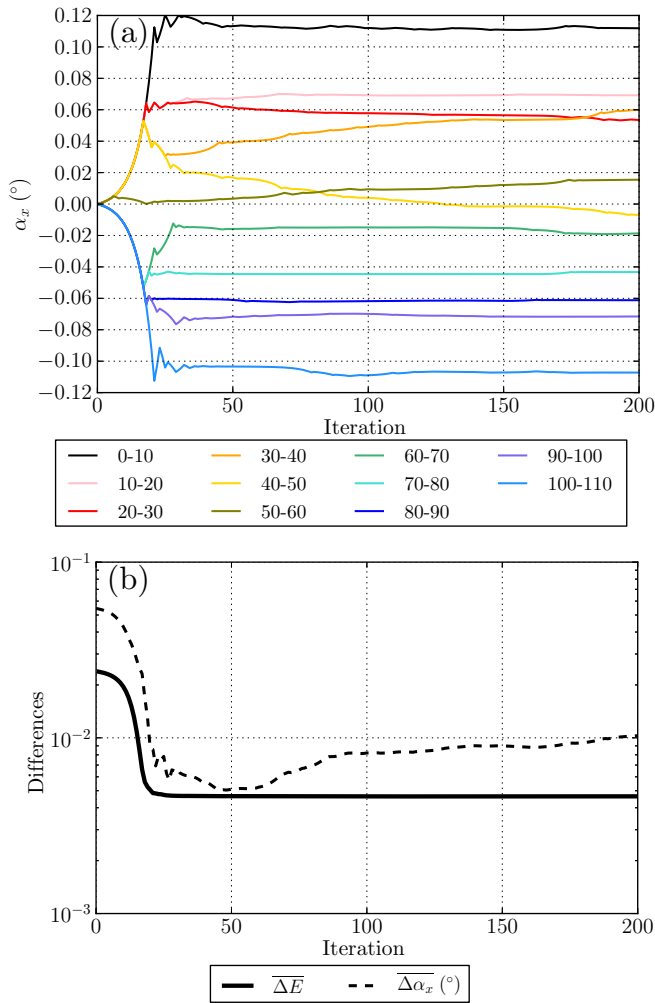


FIG. 13. PRIMES results for strain retrieval against a silicon experimental-structure-factor target including absorption at 200 kV ($n = 261$); correct values are $+0.10^\circ$ to -0.10° with 0.02° increments, showing successful parameter retrieval. (a) Individual parameter values per iteration; (b) pattern mismatch (solid) and average parameter error (dotted) per iteration.

routines like PRIMES. Other TEM data-simulation algorithms, such as atomic-resolution multislice, could run GPAW DFT simulations on thin films (like those used for mean inner potentials [21]) and potentially solve for three-dimensional atomic positions and charge densities [50,51] while fully including surface effects. It is now computationally feasible to integrate DFT into initial TEM analysis, replacing IASF models, instead of post-facto comparison [8]. We note that previous studies have shown that DFT’s utility will likely be material dependent and that electronic structure could contribute to the Stobbs-factor (high-resolution TEM image mismatch) [10,52]. Thus, DFT should be at least assessed when considering accurate TEM image or diffraction simulations, especially when direct fitting is not feasible. For DFT codes, in two dimensions, experimental scattering factors can be another DFT-quality metric [36]. DFT-TEM advantages are even greater in three dimensions, where our parameter-retrieval algorithm, PRIMES, can decipher non-minimum-energy structures extending over tens or hundreds of nanometers. For materials with nanoscale

domains, PRIMES presents a versatile framework for applying DFT in an experimentally verifiable geometry. This algorithm combines DFT nanoscale self-consistency and TEM mesoscale verifiability, enabling further three-dimensional nanoscale materials physics research.

While we treat both elastic and inelastic scattering in this paper, we use *ab initio* DFT simulations for elastic scattering but less accurate Bird-King models for inelastic scattering. These ground-state DFT simulations provide an *ab initio* model for elastic scattering, which is by far the largest single component to the structure factor at accelerating voltages typically applied in standard TEMs [34]; inelastic scattering is a much smaller effect requiring a different model. Practically, for high-energy electrons, the inelastic magnitudes are typically much smaller than the elastic ones with a different angular dependence (e.g., for silicon, $|V'/V| = 0.020_{111}, 0.031_{220}$) [34], so the common approach of a fixed absorption multiplier ($|V'/V| = \text{constant}$) is questionable [2]. Improved physical models (e.g., that of Bird and King, which includes thermal diffuse scattering through an Einstein model and excludes i.a. phonon effects [47]) are similar to experimentally fitted values [34]; unfortunately, precise and direct fits of inelastic components are more difficult due to their small magnitude, although the cross section increases with atomic number [53,54]. Conceptually, elastic scattering corresponds to a ground state specimen interaction, but inelastic scattering involves energy transfer, thus requiring a non-ground-state simulation outside the scope of this paper. Therefore, this work focuses on *ab initio* elastic scattering because it is the most important single component and provides a clear improvement over IASF models, while *ab initio* inelastic scattering is a potential subject for future research using different simulation methods.

For future work, multiple pathways exist for integrating these DFT and PRIMES methods with improved inelastic scattering models. Our absorptive structure factors are based on Einstein-model isotropic thermal diffuse scattering (TDS) parametrizations at low angles as calculated by Bird and King [47]. This physical model can be improved by using *ab initio* phonon calculations [55]. In addition to influencing structure factors, some of the “absorbed” electrons are actually measured on the detector, even if the measurement is energy filtered. This TDS intensity influences the diffraction data, and multiple approaches exist for, e.g., pattern-intensity derivative fitting [56,57] or multislice supercell ensembles of TDS thermal-displacement configurations, including potentially using *ab initio* phonon information [58]. However, TDS simulations are computationally intensive. Thus, a noniterative pre-processing step where the TDS contribution is pre-calculated and removed may be sufficient, or the TDS compensation could update only when the PRIMES specimen has greatly changed. Of course, leaving TDS intensity uncompensated implicitly treats that intensity as noise and would generally result in an increased background in diffraction data and thus decreased PRIMES performance. In summary, for future work, TDS integration options include both improved absorptive structure factors and TDS intensity quantification, as either a pre-processing step or part of an iterative routine like PRIMES.

In a broader context, the work described here is a necessary prerequisite to be able to analyze experimental data using PRIMES, because TEM specimen models are, by necessity,

approximations. A model that provides exactly accurate elastic structure factors would also provide the exactly accurate ground-state electron density—i.e., a perfect electronic-structure calculation. Therefore, it is important to demonstrate that PRIMES does not rely on a perfect structure factor model, which we showed here in Sec. II D. These tests use simulated data because the target specimen must be exactly known to determine the PRIMES result’s accuracy, especially when the structure-factor models are different. PRIMES passes these tests—in the strain case, with parameter error around 0.01° —meaning that its structure-factor models, while imperfect and open to improvement, are still good enough for PRIMES with DFT to be useful for experimental data, and PRIMES with DFT is a substantial improvement over PRIMES with IASF models.

IV. CONCLUSIONS

In this paper, we report a combination of DFT and TEM to improve both TEM and DFT simulation techniques. The GPAW DFT code is shown to be a good match for TEM—fast, accurate, and its all-electron densities can be integrated into advanced algorithms. We verified its accuracy by comparing against experimental measurements of elastic structure factors for Si, where DFT substantially outperformed IASF models, and we found close correspondence between structure factors generated using different DFT codes for multiple

materials. We then demonstrated that PRIMES (our iterative three-dimensional structural characterization algorithm) can use DFT structure factors for nanoscale self-consistency and mesoscale verifiability. We retrieved nanoscale BaTiO_3 domains of depth-resolved atomic polarization from simulated data and depth-resolved silicon strain configurations also from simulated data including experimentally derived structure factors. Future work should focus on applying DFT, especially GPAW DFT, to a wider variety of TEM simulations, including its applicability to modeling absorption, Debye-Waller factors, and frozen-lattice/phonon effects. This should also include using DFT for routine TEM simulations, given how feasible realistic electronic structure calculations can be. Future work should also include using TEM methods as a way to apply DFT to mesoscale structures, including three-dimensional objects.

ACKNOWLEDGMENTS

R.S.P. gratefully acknowledges German Research Foundation (DFG) funding under Grants No. SFB 951 and No. PE 2500/1-1 (PolaRIS-3D). C.C., S.E., and F.P. also acknowledge funding by the Spanish research project MAT2016-79455-P, and the WIEN2k simulations were carried out in the LUSITANIA II supercomputer located in Cáceres, a node of the Spanish supercomputing net (Red Española de Supercomputación—RES).

-
- [1] M. Knoll and E. Ruska, *Z. Phys.* **78**, 318 (1932).
 [2] D. B. Williams and C. B. Carter, *Transmission Electron Microscopy*, 2nd ed. (Springer, New York, 2009).
 [3] R. M. Martin, *Electronic Structure: Basic Theory and Practical Methods* (Cambridge University Press, Cambridge, UK, 2004).
 [4] P. A. Doyle and P. S. Turner, *Acta Crystallogr. Sect. A* **24**, 390 (1968).
 [5] I. Lobato and D. Van Dyck, *Acta Crystallogr. Sect. A* **70**, 636 (2014).
 [6] M. Hýtch, F. Houdellier, F. Hüe, and E. Snoeck, *Nature (London)* **453**, 1086 (2008).
 [7] K. Tsuda, A. Yasuhara, and M. Tanaka, *Appl. Phys. Lett.* **103**, 082908 (2013).
 [8] J. M. Zuo, M. Kim, M. O’Keeffe, and J. C. H. Spence, *Nature (London)* **401**, 49 (1999).
 [9] A. Rother, M. Reibold, H. Lichte, T. Leisegang, A. A. Levin, P. Paufler, D. C. Meyer, S. Gemming, I. Chaplygin, G. Seifert, A. Ormeci, and H. Rosner, *Phys. Rev. B* **74**, 134116 (2006).
 [10] B. Deng and L. D. Marks, *Acta Crystallogr. Sect. A* **62**, 208 (2006).
 [11] J. Ciston, J. S. Kim, S. J. Haigh, A. I. Kirkland, and L. D. Marks, *Ultramicroscopy* **111**, 901 (2011).
 [12] L. D. Marks, A. N. Chiaramonti, S. U. Rahman, and M. R. Castell, *Phys. Rev. Lett.* **114**, 226101 (2015).
 [13] S. Borghardt, F. Winkler, Z. Zanolli, M. J. Verstraete, J. Barthel, A. H. Tavabi, R. E. Dunin-Borkowski, and B. E. Kardynal, *Phys. Rev. Lett.* **118**, 086101 (2017).
 [14] J. J. Mortensen, L. B. Hansen, and K. W. Jacobsen, *Phys. Rev. B* **71**, 035109 (2005).
 [15] J. Enkovaara, C. Rostgaard, J. J. Mortensen, J. Chen, M. Duřak, L. Ferrighi, J. Gavnholt, C. Glinsvad, V. Haikola, H. A. Hansen, H. H. Kristoffersen, M. Kuisma, A. H. Larsen, L. Lehtovaara, M. Ljungberg, O. Lopez-Acevedo, P. G. Moses, J. Ojanen, T. Olsen, V. Petzold, N. A. Romero, J. Stausholm-Møller, M. Strange, G. A. Tritsarlis, M. Vanin, M. Walter, B. Hammer, H. Häkkinen, G. K. H. Madsen, R. M. Nieminen, J. K. Nørskov, M. Puska, T. T. Rantala, J. Schiøtz, K. S. Thygesen, and K. W. Jacobsen, *J. Phys.: Condens. Matter* **22**, 253202 (2010).
 [16] R. S. Pennington, W. Van den Broek, and C. T. Koch, *Phys. Rev. B* **89**, 205409 (2014).
 [17] R. S. Pennington and C. T. Koch, *Ultramicroscopy* **148**, 105 (2015).
 [18] R. S. Pennington and C. T. Koch, *Ultramicroscopy* **155**, 42 (2015).
 [19] M. Y. Kim, J. M. Zuo, and J. C. H. Spence, *Phys. Status Solidi A* **166**, 445 (1998).
 [20] P. Kruse, M. Schowalter, D. Lamoen, A. Rosenauer, and D. Gerthsen, *Ultramicroscopy* **106**, 105 (2006).
 [21] R. S. Pennington, C. B. Boothroyd, and R. E. Dunin-Borkowski, *Ultramicroscopy* **159**, 34 (2015).
 [22] H. Bethe, *Ann. Phys. (Berlin)* **392**, 55 (1928).
 [23] C. H. Mac Gillavry, *Physica* **7**, 329 (1940).
 [24] K. Ishizuka and N. Uyeda, *Acta Crystallogr. Sect. A* **33**, 740 (1977).
 [25] P. B. Hirsch, A. Howie, R. Nicholson, D. W. Pashley, and M. J. Whelan, *Electron Microscopy of Thin Crystals*, 2nd ed. (Robert E. Krieger Publishing Co., Malabar, FL, 1977).
 [26] K. Ishizuka, *Acta Crystallogr. Sect. A* **38**, 773 (1982).
 [27] K. Kambe, *Ultramicroscopy* **10**, 223 (1982).
 [28] S. R. Bahn and K. W. Jacobsen, *Comput. Sci. Eng.* **4**, 56 (2002).
 [29] D. K. Saldin and J. C. H. Spence, *Ultramicroscopy* **55**, 397 (1994).

- [30] J. C. H. Spence and J. M. Zuo, *Electron Microdiffraction* (Plenum Press, New York, NY, 1992).
- [31] M. Ohtsuka, T. Yamazaki, I. Hashimoto, and K. Watanabe, *Acta Crystallogr. Sect. A* **65**, 135 (2009).
- [32] R. S. Pennington, F. Wang, and C. T. Koch, *Ultramicroscopy* **141**, 32 (2014).
- [33] J. M. Zuo, P. Blaha, and K. Schwarz, *J. Phys.: Condens. Matter* **9**, 7541 (1997).
- [34] Y. Ogata, K. Tsuda, and M. Tanaka, *Acta Crystallogr. Sect. A* **64**, 587 (2008).
- [35] J. M. Zuo, *Acta Crystallogr. Sect. A* **49**, 429 (1993).
- [36] J. Friis, G. K. H. Madsen, F. K. Larsen, B. Jiang, K. Marthinsen, and R. Holmestad, *J. Chem. Phys.* **119**, 11359 (2003).
- [37] F. Wang, R. S. Pennington, and C. T. Koch, *Phys. Rev. Lett.* **117**, 015501 (2016).
- [38] A. Lubk, E. Javon, N. Cherkashin, S. Reboh, C. Gatel, and M. Hÿtch, *Ultramicroscopy* **136**, 42 (2014).
- [39] H. W. King, *CRC Handbook of Chemistry and Physics, 89th Edition: Crystal Structures and Lattice Parameters of Allotropes of the Elements* (CRC Press, Boca Raton, 2008).
- [40] I. Lobato and D. Van Dyck, *Ultramicroscopy* **155**, 11 (2015).
- [41] G. H. Kwei, A. C. Lawson, S. J. L. Billinge, and S. W. Cheong, *J. Phys. Chem.* **97**, 2368 (1993).
- [42] E. Gabriel, G. E. Fagg, G. Bosilca, T. Angskun, J. J. Dongarra, J. M. Squyres, V. Sahay, P. Kambadur, B. Barrett, A. Lumsdaine, R. H. Castain, D. J. Daniel, R. L. Graham, and T. S. Woodall, in *Proceedings, 11th European PVM/MPI Users' Group Meeting* (Budapest, Hungary, 2004), pp. 97–104.
- [43] C. T. Koch, *Ultramicroscopy* **111**, 828 (2011).
- [44] J. P. Perdew, K. Burke, and M. Ernzerhof, *Phys. Rev. Lett.* **77**, 3865 (1996).
- [45] Y. Zhang and W. Yang, *Phys. Rev. Lett.* **80**, 890 (1998).
- [46] B. Hammer, L. B. Hansen, and J. K. Nørskov, *Phys. Rev. B* **59**, 7413 (1999).
- [47] D. M. Bird and Q. A. King, *Acta Crystallogr. Sect. A* **46**, 202 (1990).
- [48] L. Kleinman, *Phys. Rev. B* **24**, 7412 (1981).
- [49] G. K. H. Madsen, P. Blaha, K. Schwarz, E. Sjöstedt, and L. Nordström, *Phys. Rev. B* **64**, 195134 (2001).
- [50] W. Van den Broek and C. T. Koch, *Phys. Rev. Lett.* **109**, 245502 (2012).
- [51] W. Van den Broek and C. T. Koch, *Phys. Rev. B* **87**, 184108 (2013).
- [52] M. Hÿtch and W. Stobbs, *Ultramicroscopy* **53**, 191 (1994).
- [53] D. M. Bird and M. Saunders, *Ultramicroscopy* **45**, 241 (1992).
- [54] R. Egerton and K. Wong, *Ultramicroscopy* **59**, 169 (1995).
- [55] F. Giustino, *Rev. Mod. Phys.* **89**, 015003 (2017).
- [56] P. N. H. Nakashima, A. E. Smith, J. Etheridge, and B. C. Muddle, *Science* **331**, 1583 (2011).
- [57] P. N. H. Nakashima and B. C. Muddle, *Phys. Rev. B* **81**, 115135 (2010).
- [58] D. A. Muller, B. Edwards, E. J. Kirkland, and J. Silcox, *Ultramicroscopy* **86**, 371 (2001).